MAPPING AND DETECTION OF HOTSPOT SOURCES FROM INDUSTRIAL AREA HEAT (IAH) USING AERIAL AND SATELLITE-BASED TIR DATA IN PASIR GUDANG

Mohammed Dahiru Zakari[1,2,3], Mazlan Hashim[1, 2*], NoorDyana Hassan[1, 2]

[1]Geoscience & Digital Earth Centre (INSTEG), Research Institute for Sustainable Environment (RISE), Universiti Teknologi Malaysia, Johor Bahru, Malaysia

[2]Faculty of Geoinformation & Real Estate, Universiti Teknologi Malaysia, Johor Bahru, Malaysia

[3]Adamawa State Polytechnic, Yola. Adamawa State Nigeria

*E-Mail: zakari722@gmail.com:mazlanhashim@utm.my: noordyana@utm.my

Commission 4, WG 7

KEY WORDS: Aerial and satellite-based, Thermal Infrared Sensors, Industrial area heat, Hot-spot sources, Normalized vegetation index.

ABSTRACT:

When assessing the state of the climate system, industrial area heat (IAH) is one of the most critical variables for energy auditing. Thermal infrared (TIR) remote sensing techniques were used to track the surface temperature and microclimate impacts in an industrial environment by analysing in-situ data and their relationship with industrial features to characterise their impacts on human health and climate change. Based on TIR data, this study used an automatic detection method for industrial area heat (IAH). The IAH data is first retrieved, then the local abnormal high-temperature pixels are extracted using PIX4D software for UAV and split window for Landsat 8, and finally, the hotspot targets are identified using the spatial autocorrelation Moran's analysis tool available in the ArcGIS ESRI environment. The correlations (R2) between in-situ measurement and satellite-based industrial emissions at PGI were 0.85 with an RMSE of + 3.37 and 0.89 with an RMSE of + 1.42 at KSM. The detection accuracy of IAH methods is dominant. IAH accounted for 20% of the cool- and hot spots areas in the entire study area. The total cool-spots had a higher polygons per km2 (3.5 n/km2) value than the total hot-spots (0.6 n/km2) value, while LEVEL-3 and LEVEL-2 had the lowest values, while the highest values were always found in LEVEL-1, with approximately 50 % IAH variation between the previous and next level. Moving from the total average cool-spot to the total average hot-spot classes generally increased about 5 °C. Between the most extreme cool- and hot-spot levels (LEVEL-3) for PG in the overall industrial area, a mean IAH increase of approximately 34.7 °C and 58.5 °C was observed.

1. Introduction

A remote sensing-based approach for mapping and estimation of IAH is fast recognized as the only viable tool for retrieval of land surface temperature (LST) over a large area (Biswal et al., 2019). It offers an opportunity to collect relevant data from various sectors at high spatial and temporal resolutions with spectral scales (Liu et al., 2018; Zhang et al., 2019). Currently, in an epoch of technological revolution, progress in data acquisition is quite crucial and remained relevant in the thermal domain. However, the influence of IAH in economic sectors and vigorous heat loss from industrial plants have substantial implications for human health and climate change (Vollath, 1987). Existing high-temperature detection methods are still limited when it comes to detecting small-scale industrial area heat (IAH) with a focus on hotspot targets because the well-behaved process (contextual algorithm) is time-consuming and complex (Xia et al., 2018) and relies heavily on midinfrared (Kuenzer et al., 2013) or short- infrared data (Malakar et al., 2018).

However, the most widely used data with mid-infrared or short-infrared channels for heat detection have low spatial resolutions (Pandya et al., 2014; Pour et al., 2019; Yang et al., 2017). Furthermore, medium and high spatial resolution data, such as Unmanned area vehicles (UAV) and Landsat 8 TIRS, are primarily obtained during the day, since daytime data area ideal (Heutger, 2014; Murad et al., 2019; Omotosho et al., 2015). When compared to low-resolution thermal data, Landsat 8 data has a high sensor sensitivity in the TIR region with a spatial resolution of 100 m resample to 30 m (Mia et al., 2017), implying a higher brightness temperature saturation and the possibility of discovering cooler or smaller hot spots. Landsat 8 data have two TIR channels ranging from 10.8 to 12 m, which compensate for the lack of midinfrared and SWIR channels (Hazaymeh & Hassan, 2015; Storey et al., 2014), which are not always available at night (Xia et al., 2018). We present a simple thermal variance index (TVI) based on Wien's law and Planck's law for the rapid detection of thermal variance information using Landsat 8 TIR data (Kant, 2021).

Even though remotely sensed-based studies provide an alternative for the accurate depiction of IAH (Xia et al., 2018; Zhang et al., 2019), this research is limited to industrial applications. The use of remotely sensed surface temperature allows data to be collected over relatively large areas. Even the spatial resolution of such datasets, which ranges from 60 m to 1000 m, is inadequate in acquiring local exchanges of surface temperature related to various environmental features in metropolises (Zheng & Weng, 2018). Therefore, UAV-based techniques can capture thermal imagery with a very high spatial resolution (≥ 5~10). These studies were supplemented by using disruptive technology to map and identify hotspot targets. These were accomplished by retrieving and estimating heat loss using UAV and Landsat-8 data, and (ii) identifying the hotspot target above ambient temperature. (iii) Relate the UAV to the satellite map. This study has a significant impact on the energy balance because it examines the relationship between industrial

materials and thermal energy at microscales (1:50,000 ~ 100,000 scales. Therefore, detecting and mapping energy loss within various ranges of targets for various temperatures will help policymakers understand how to improve disparities in existing industrial substances.

The main objective of this study is to use the SW algorithm for IAH retrieval from Landsat 8 TIRS data via GIS software and UAV TIR data via PIX4D software to display how the analysis and distribution of surface temperature for industrial areas are carried out for quantifying and mapping IAH. The application is in the industrial area of Pasir Gudang, Peninsular Malaysia. The stages to be realised are as follows: first, we present the algorithm derivation and computation analysis for the brightness temperature (TB) for retrieving IAH, and then IAH from UAV is directly extracted using PIX4D software. The multispectral (4,5, and 6) indices were used to track the evolution of the industrial area emissivity (IAE), and the TIRS bands (10 and 11) from Landsat 8 were used to retrieve IAH. The SW algorithm estimates the IAH for each ground pixel by combining the TB and IAE. Second, we validate the proposed algorithm and UAV data output by correlating them with in-flight air temperature data. Most importantly, it will help to accelerate the implementation of Targets 9.4 and 11.6 to retrofit industries to make them more sustainable. As a result, it will make a significant contribution to the achievement of SDGs 9.4 and 11.6 by 2030, which emphasise the need to promote resource-use efficiency and minimise cities' environmental impact by paying special attention to municipal waste management.

2. Materials and methods

2.1. Study Area

The Pasir Gudang industrial area (1°30' N, 103°56' E) is Johor state's largest industrial base and comprehensive centre in southern Peninsular Malaysia (Figure 1). It is located in the tropical zone, which is influenced by two monsoon seasons: The Southwest monsoon, which occurs from late May to September, and the Northeast monsoon, which occurs from November to March. The Northeast Monsoon brings heavy rain, particularly to Peninsular Malaysia's east coast states and western Sarawak, whereas the Southwest Monsoon usually brings relatively dry weather (Suhaila et al., 2010).

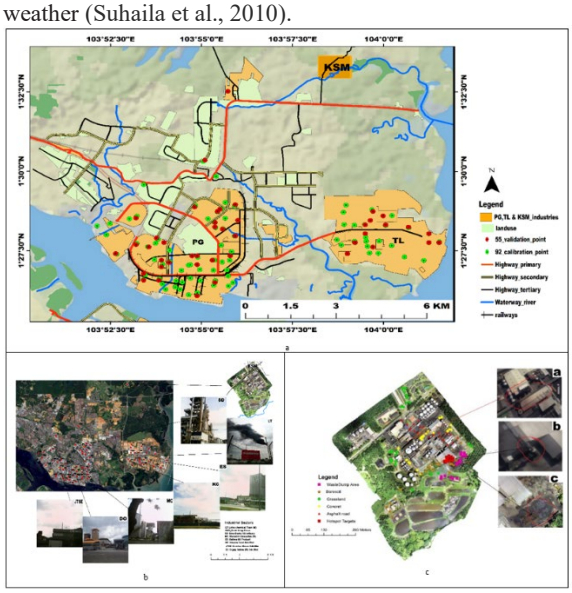

Figure 1. The study area

3. Method for retrieving IAH from UAV and Landsat 8

There are several algorithms for the retrieval of surface temperature (SC, MW SW and Dual-channel), however, for this study we employed SW for the retrieval of IAH developed by Sobrino et al. (2001) for Landsat 8. According to Rogninn et al. (2015), we adopted the SW algorithm in the following form for IAH retrieval from L8 TIRS (B10 &11) as shown in Figure 2 methodological flow chart.

3.1 IAH retrieval from UAV

The FLIR conversion procedure to generate radiometrically calibrated JPEG photos in bulk include Stage 1) one image of the blackbody object and the surrounding features was acquired using an infrared thermometer operating on a 9V 6F22 battery. Its absolute measurement accuracy is ±1.0 ◦C and its thermal sensitivity is 0.1 ◦C. stage 2) the acquired radiometric JPEG image from the UAV was loaded into FLIR Tools software combined with relevant environmental parameters (air temperature, humidity, emissivity) (Sagan et al., 2019) measurements during the task.

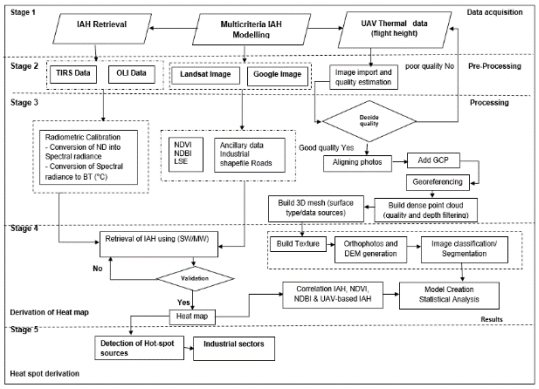

Figure 2. The method flowchart for retrieving IAH

Then the converted and retrieved temperature values were exported to TXT files (Zhang et al., 2018). The bias between the blackbody object and the surrounding temperature was also realized. Stage 3) Radiant heat temperatures were extracted from UAV photos and related to the locations of in situ data as shown in (Figure 2.) which brings about the linear regression model being used as a radiometric calibration comparison. Stefan-law Boltzmann's equation describes the relationship between radiant and surface temperatures, which is determined by emissivity and incoming longwave radiation (Li et al., 2013).

$$T_s = \sqrt[4]{\frac{\sigma T_{rad}^4 - (1-\varepsilon) LW\downarrow}{\varepsilon\sigma}} \qquad (1)$$

where Ts denotes the surface temperature (K), Trad the radiant temperature (K), emissivity, the Stefan-Boltzmann constant (5.67 10^{-8}), and LW the incoming longwave radiation (W m^{-2}).

3.2 IAH retrieval from Landsat 8

Landsat 8 TIRS remote sensing data products from the US Geological Survey were used to create the IAH identification layer for this study (Khalil et al., 2017; Micijevic et al., 2016)(https://earthexplorer.usgs.gov) and UAV thermal data (Kraaijenbrink et al., 2018; Maes et al., 2017; Pérez-García et al., 2018; Song & Park, 2020), referred to the summer period (September) 2020. IAH was estimated from clear-sky images with a horizontal resolution of 30 m (the US Geological Survey resampled the TIRS bands' initial resolution of 100 m to 30 m)

(10:30 UTC) (Rozenstein et al., 2014). BT is the electromagnetic radiance moving upward from the top of the earth's atmosphere to allow the thermal calibration conversion (The DN values of TIR band 10 and 11 to TOA spectral radiance), (USGS Handbook, 2013) equation 1. thus, The BT is not a temperature on the ground rather is the temperature at the satellite. The thermal band is first converted from DN to at-satellite radiance and then to effective at-satellite temperature (T), Assuming surface emissivity = 1 to convert radiance to temperature was used like the following equation 2 & 3 (Disast et al., 2016; Rongaliet al., 2018).

$$L_\lambda = Gain_\lambda \times DN_{cal} + A_L - Q_i\,(Bias_\lambda) \quad (2)$$

$$T_B = \Big/ Ln\left[\left(\frac{K_1}{L_\lambda}\right)+1\right] - 273.15 \quad (3)$$

where: T_B- At satellite brightness temperature (K); K_1- Calibration constant 1 $(watts/(m^2 srad * \mu m))$; K_2 -Calibration constants 2, However, the values are in Kelvin (K), to have it in Celsius degree, it is necessary to consider adding absolute zero which is equal to -273.15.

3.3 Normalized difference vegetation index (NDVI)

To transform multispectral data into a single image band representing the distribution of vegetation/build area, NDVI was used. The NDVI values represent the pixel quantity of green vegetation; the NDVI is determined from the visible and near-infrared light reflected by vegetation (Malik et al., 2019; Tang et al., 2015). Using the ArcGIS 10.5 software, NDVI maps are extracted from Landsat-8 images as follows in Equ. 4:

$$\mathrm{NDVI} = \frac{\mathrm{NIR(band5)-R(band4)}}{\mathrm{NIR(band5)+R(band4)}} \quad (4)$$

Where, In the Landsat-8 red and near-infrared bands the NIR and Red are the spectral reflection, NDVI calculations often fall between ranges -1 and +1 for a single pixel; Where more green vegetation signifies positive values and the negative values denote bare land surface characteristics.

3.4 Industrial Surface Emissivity (ISE)

This was considered phase 4 to determine the ISE, where the emissivity of the land surface is calculated using the NDVI image-based process (Nguyen et al., 2019; Saradjian & Jouybari-Moghaddam, 2019; Valor & Caselles, 1996). Images of the fractional vegetation cover (FVC) were generated. This can, however, be applied by using Equa.5.

$$\mathrm{FVC} = \frac{\mathrm{NDVI} - NDVI_{soil}}{NDVI_{veg} - NDVI_{soil}} \quad (5)$$

The industrial area emissivity images of bands 10 and 11 are then explicitly used to measure the average and variations in emissivity (Equations 7 and 8). Thus, using Equation 6, the land surface emissivity images of bands 10 and 11 are created separately.

$$LSE = \varepsilon_s \times (1 - FVC) + \varepsilon_v \times FVC \quad (6)$$

Where; LSE is the surface emissivity; ε_s *and* ε_v represent the emissivity of pure vegetation and pure soil areas respectively, and FVC represent the fractional vegetation cover (surface roughness) (Cristo & Jime, 2009; Julien et al., 2011; Sobrino et al., 2008). However, in equation 11, the mean LSE images of TIRS 10 and 11 are combined by using Equa.7 and 8.

$$LSE_{mean} = \frac{\mathrm{LSE_{10}} + LSE_{11}}{2} \quad (7)$$

$$\Delta_{mean} = \mathrm{LSE_{10}} - LSE_{11} \quad (8)$$

3.5 The retrieval of Industrial Area Heat (IAH)

The SW algorithm applied in this study is also referring to the multi-channel approach and used the different absorptions of two TIR bands, linearizing or non-linearizing RTE concerning the temperature (S. Zhang et al., 2019). As reported by (Zhang et al., 2019), the SW algorithm employed in this study is estimated as;

$$T_s = T_{B10} + 1.378(T_{B10} - T_{B11}) + 0.183(T_{B10} - T_{11})^2 - 0.268 + (54.3 - 2.238w)(1-\varepsilon) + (-129.2 + 16.4w)\Delta\varepsilon \quad (9)$$

where T_{B10} and T_{B11} are the at-sensor brightness temperatures at the bands (10 and 11) in Kelvins, ε is the mean emissivity, ε = 0.5(ε_{t10} + ε_{t11}), Δε is the emissivity difference, Δε =(ε_{t10} - ε_{t11}), *w* is the total atmospheric water vapour content (in g·cm^{-2}). Though, both SW and SC algorithms require the water vapour content (*w*) in the atmosphere as input.

Constants	c_0	c_1	c_2	c_3	c_4	c_5	c_6
Value	-0.268	1.378	0.183	54.300	-2.238	-129.200	16.400

Table 1. SW coefficients values for TIRS bands of Landsat-8 imagery

3.6. The Industrial Thermal Area Index (ITAI) Layer

Following the estimation of IAH, the industrial thermal area Index (ITAI) was chosen to apply an industrial sector evaluation based on thermal conditions. This measurement has been used in several recent studies to estimate the impact of various environmental factors on the quality of life in cities(Guerri et al., 2021; Guha & Govil, 2021; Guha et al., 2018; Liu & Zhang, 2011; Portela et al., 2020; Renard et al., 2019). To estimate ITAI, which was used to quantitatively explain the industrial effect, the following equation was used:

$$\mathrm{ITAI} = \frac{(\mathrm{T_s} + \mathrm{T_{mean}})}{\mathrm{T_{mean}}} \quad (10)$$

Where $THVI$ represents the industrial heat variance index, h_s is the heat emission of the ith pixel in the industrial area, and h_{mean} is the average heat emission of industries, including surrounding areas, at the time the satellites overpass.

3.6.2. Thermal Hot-Spot Detection

The hotspot analysis used in this study was created to identify industrial hotspot sources based on different sector emissions with spatially widespread IAH values, resulting in positive or negative structural IAH anomalies. The criterion for identifying a statistically significant hot spot or cool spot (Jamei *et al.*, 2019) values at the local level is the highest and lowest value surrounded by other features with similar IAH values. The analyses were carried out using the ArcGIS ESRI environment's Hot-Spot Analysis tool (Getis-Ord Gi*) (Lanorte et;., 2012). Daytime IAH datasets from Landsat 8 images that had been converted to a spatial point object were used to evaluate the method. The Getis-Ord Gi* statistic method was used to calculate each IAH point in the context of its neighbouring points. Significant hot- and cool-spot areas were defined spatially using the formula described by (Yongjiu et al., 2018):

$$G_i^* = \frac{\sum_{j=1}^{n}\omega_{i,j}x_j - \overline{X}\sum_{j=1}^{n}\omega_{i,j}}{s\sqrt{\frac{\left[n\sum_{j=1}^{n}\omega_{i,j}^2 - (\sum_{j=1}^{n}\omega_{i,j})^2\right]}{n-1}}} \quad (11)$$

$$\sum_{j=1}^{n} \omega_{i,j} x_j$$

Where, x_j represent the attribute value for the feature j; $\omega_{i,j}$ represent the spatial weight between feature i and j; n is equal to the total number of features. X and S are mean and variance values, respectively:

$$\bar{X} = \frac{\sum_{j=1}^{n} x_j}{n} \quad (12)$$

$$s\sqrt{\frac{\sum_{j=1}^{n} x_j^2}{n} - (\bar{X})^2} \quad (13)$$

4. Results and Analysis

This study presented four outputs: (1) UAV retrieved IAH map, (2) Satellite-based using Landsat 8 retrieve IAH map, (3) identified IAH hotspot targets, and (4) regression analysis for In-Situ, UAV, and Satellite-based.

4.1. Results and Analysis Based on Satellite Data

In this study, in-situ observations were used to verify the final retrieved IAH results due to a lack of simultaneous land surface temperature data when the satellite passes. The mean temperature of retrieved IAH for PG from Landsat 8 data is 41.4 °C, the mean ambient temperature is 35.6 °C, the Std. is 7.2, and the mean in-Situ observation is 61.4 °C. The correlation coefficient is 0.88 with an RMSE of (2.5 °C) for the PGIA, while the mean temperature of retrieved IAH for KSM is 38 °C), the mean ambient temperature is 37.16 °C), the Std. is 6.8, and the mean in-Situ is 63.79 °C. The correlation coefficient is 0.87, with an Std. of (2.6 °C). As shown in Figure 5, the SW retrieving method from Landsat 8 data was used with greater accuracy, resulting in high-quality retrieved IAH data for the analysis of industrial area heat. The mean temperature of retrieved IAH is 38 °C, the mean ambient temperature is 37 °C, and the mean in-Situ observation on 20 September 2020 is 63.8 °C, Std. is 8.2. For the Oil Palm Industrial area, the correlation coefficient is 0.74, with an IAH RMSE of (1.4 °C). Although the IAH of the study areas for Landsat 8 and UAV were not the same, their change trend is very close, particularly for air and UAV temperature, as shown in Tables 3 and 4. The spatial consistency of the Landsat 8 retrieving maximum heat of 89.8 °C with an error of (3 °C) and the UAV retrieving maximum heat of 143.3 °C with an error of (1.4 °C) indicated that the two sensors are comparable to IAH retrievals in the Peninsular Malaysia case study. However, the comparison of the two sensors should be investigated further with more data collection soon. The heat emission in the Pasir Gudang estate's industrial sectors (Pasir Gudang and Keck Seng Masai Oil Palm) was higher than 89 °C for Landsat and higher than 140 °C for UAV at Keck Seng Masai. These industries are the most affected by IAH. The temperature in all industrial sectors ranged between 60 and 90 °C, with industrial sectors being the dominant factor. It should also be noted that, due to the scattered distribution of heat from satellite-thermal emission, the effects of IAH spread evenly but do not yet form a large-scale regional heat effect. Although satellite data (Landsat 8 and UAV thermal band data) can be used to investigate the extreme heat emission distribution of IAH in highly targeted industrial sectors, the method for calibrating IAH in future studies will need to be refined with in situ observation of IAH.

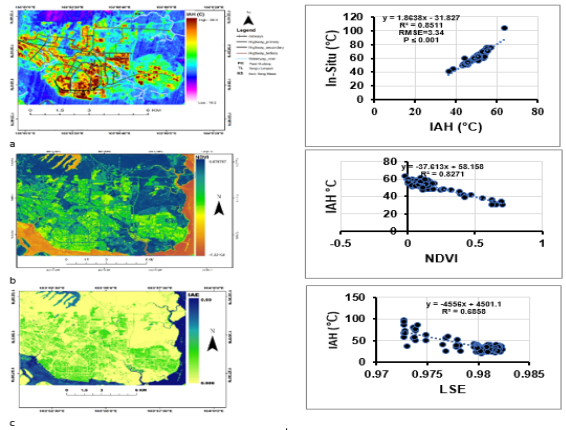

Figure 5. Spatial distribution of IAH and surface indices for Pasir Gudang.

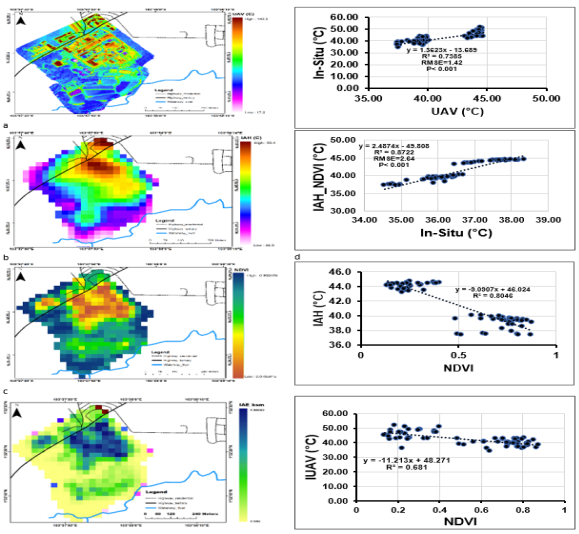

Figure 6. Statistical distribution for regression coefficient (a) for the vegetation Cover responses; and (b) Built-up cover responses taking over Keck Seng Oil Palm Industry

		Industrial area heat Emission (°C)				Factors (normalized)	
		Amb. Temp	In-Situ	IAH_NDVI	IAH	NDVI	LSE
PG	Min	30.3	41.3	19.152	18.595	-1.331	0.974
	Mean	35.586	61.349	41.297	41.432	0.406	0.9854
	Max	37.4	103.43	89.861	89.766	0.8707	0.9884
	Std	± 1.291	± 8.423	± 7.259	± 7.203	± 0.41	± 0.002
	No. Sample points (n)	82	82	82	82	82	82
	R2			0.879	0.88	0.8271	
	RMSE			± 2.511	±2.5133		

Table 3. Scattered plots of (a) IAH (b) NDVI and (c) IAE map generated from Landsat-8 data acquired on the 10th and IAH vs IAE

Plot	IAH_NDVI (°C)
Number of Points	82
Degrees of Freedom	80
Intercept	21.81209 ± 1.33834
Slope	0.51365 ± 0.02161
Residual sum of squares	217.35828
Pearson's	0.93592
R-Squares	0.87595
Adj. R-Square	0.8744

Table 4. The correlation coefficient results for in-Situ Vs UAV Tir-based

The NDVI values were used as input to create the fvc image using Equations 5-6 and the IAE image using Equation 7. However, the IAHE image in Figure 4 was captured using the NDVI threshold value method and Equa.5-8. Figures 5 and 6 show NDVI and IAE raster maps. The results show that the NDVI value ranges from -1 to 0.87, with a mean of 0.41 and a standard deviation of 0.41 images. The lowest NDVI values

were observed over an industrial area (-10.43), sub-industrial areas (-0.08 0.31) with yellow colour, and higher NDVI values over vegetation and greenery areas with green and blue colour. Values close to one, on the other hand, indicate a positive response and healthy green vegetation. Furthermore, the decrease in NDVI values is attributed to land use activities with negative responses, as shown in Figure 7. For greenery areas, heat emission has a significant negative correlation with NDVI (R^2= 0.83). The industrial area emissivity (IAE) value of the map ranges from 0.086 to 0.99, indicating low emissivity when compared to the vegetation area in developed areas. High temperatures are present in the heat emission sources. It means that an area with more vegetation has a lower temperature because available energy is distributed more towards the evapotranspiration process, resulting in a lower AST when compared to a low vegetation area. Weak vegetation has a higher ambient temperature because of the low NDVI value. Previous research (Bendib et al., 2017; Jamei et al., 2019; Malik et al., 2019) has found a significant negative relationship between NDVI and IAE (Danodia et al., 2017)

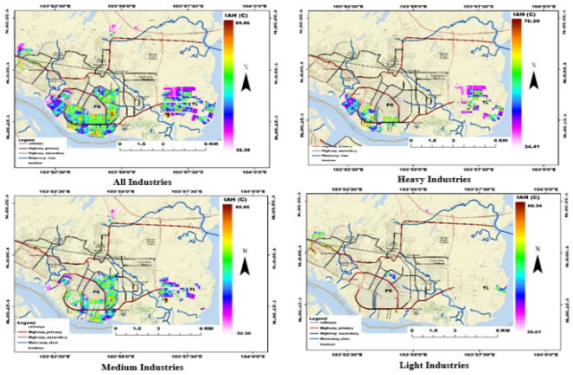

Figure 7. Showing all hotpots targets for (a) all Categories of industries (Heavy, Medium and Light (b) Heavy Industries (c) Medium Industries (d) Light Industries at Pasir Gudang

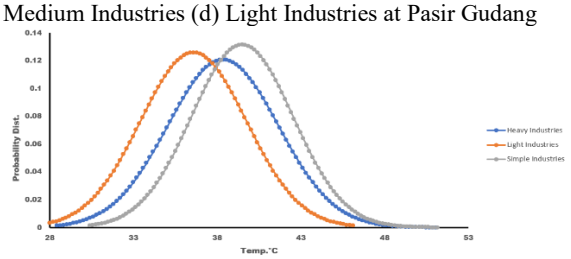

Figure 9. Normal distribution for all industries (Heavy, Light, and Simple).

Industrial area heat(°C)																
	All Industries				Heavy Industries				Medium Industries				Light Industries			
	Min.	Mean	Max.	Std	Min.	Mean	Max.	Std	Min	Mean	Max.	std	Min	Mean	Max	Std
Amb_Temp	30.3	35.59	37.4	± 1.29	32.6	35.64	37.4	± 1.32	30.3	35.56	37.4	± 1.32	36.4	36.7	36.9	± 0.22
In-Situ	51.2	67.31	112.43	± 12.01	51.2	67.94	112.2	± 14.07	51.5	68.29	112.43	± 12.37	56.77	60.46	64.6	± 3.21
IAH	32.38	51.17	89.86	± 7.56	34.41	49.48	76.29	± 6.76	32.38	52.91	89.86	± 7.91	35.01	51.46	58.34	± 6.91

Table 5. Summary result for Descriptive statistics of Thermal heat emission based on industrial types, NDVI and NDBI for Pasir Gudang Industrial Area

Industrial Sectors	Acronym	E	N	Amb. _Temp.	In_Situ	IAH (C)	IAH Model (C)
Iron and steel	I&S	103.919	1.4729	34.2	62	79.83	80.15
Iron and Steel	I&S	103.987	1.4712	36.9	67	76.58	77.20
Food and Beverage	F&B	103.921	1.4652	35.4	65.9	78.51	78.96
Chemicals Industry	CI	103.983	1.4597	37.4	108.5	82.31	82.37
Chemical and Petrochemical	C&PC	103.966	1.4603	34.3	70.4	81.09	81.28
cement, lime, construction sand, gravel	Ceramic	103.896	1.4604	36.6	69.9	78.81	79.23
Iron and steel	I&S	103.978	1.4573	33.4	75.7	88.22	87.60
Clay Product and Refractory Manufacturing	Ceramic	103.925	1.4549	35.4	71.3	76.36	77.00
Iron and Steel	I&S	103.970	1.4540	36.2	112.43	69.95	89.61
Electronic Industry)	EI	103.911	1.4523	34.1	66	77.47	78.01
Paper, Pump and Printing	PP&P	103.900	1.4504	34.1	73.1	77.14	77.71
Manufacturing, Fabrication, Eriction of stell	I&S	103.924	1.4510	35.7	63.4	76.46	77.09
Oil Palm refinery	OPR	103.908	1.4488	35.3	62.3	76.86	77.46
Iron and Steel	I&S	103.891	1.4444	35.6	72.6	80.14	80.43
Food and Beverage	F&B	103.890	1.4422	33.7	62.7	76.01	76.67
Food and beverage	F&B	103.908	1.4354	36.1	73.15	82.05	82.14
Electronic Industry	EL	103.921	1.4742	36.7	63	74.78	75.53
Non-Ferrous (Iron and steel)	Non-Ferrous	103.985	1.4667	34.4	69.4	73.16	74.00
Iron and steel	I&S	103.994	1.4657	35.9	69.5	71.75	72.65
Paper, Pump and Printing	PP&P	103.918	1.4657	35.9	69.9	73.52	74.34
Electronic Industry	EI	103.926	1.4619	36.4	68.5	74.28	75.06
Food and Beverage	F&B	103.887	1.4585	35.3	72.4	70.89	71.81
Iron and Steel	I&S	103.920	1.4578	33.5	69.8	74.46	75.22
Palm oil refinery	OPR	103.921	1.4502	36.3	66.3	70.39	71.33
Food and beverage	F&B	103.897	1.4491	36.6	60.6	69.86	70.80

Table 6. Variation of IHW (°C) for industrial sectors > 80 °C

	Temp. (°C)					
	Amb. Temp	In-Situ	UAV_Tir	IAH	NDVI	IAE
Min	32.83	37.4	17.18	26.86	0.07859	0.9860
Mean	37.16	63.79	37.99	40.04	0.6532	0.9862
Max	40.2	250	143.33	55.38	0.9682	0.9866
Std	± 1.87	43.12	± 8.16	± 6.78	± 0.2504	0.00
No. Sample points (n)	143	143	143	143	143	
Temp.(°C)	37.16 ± 1.83	63.79 ± 43.121	35.106 ± 10.53	39.759 ± 6.826	0.5253 ± 0.2042	
R^2			0.738	872	0.805	
RMSE			± 1.42	± 2.64		

Table 7. Statistical spatial distribution for Keck Seng field data

Plot	IAH_NDBI (°C)	UAV_Tir (°C)
Number of Points	72	72
Degrees of Freedom	70	70
Intercept	22.14008 ± 0.66196	-13.68894 ± 3.98947
Slope	0.35065 ± 0.01604	1.36227 ± 0.08594
Residual sum of squares	8.66592	320.08594
Pearson's	0.93391	0.85938
R-Squares	0.87219	0.73853
Adj. R-Square	0.87037	0.73479

Table 8. The correlation coefficient results for in-Situ Vs UAV Tir-based

4.2. The Industrial Thermal Area Index (ITAI) Layer

Table 9 and Figure 8 show the extreme levels of industrial assessment: excellent (0) and worst (> 0.016) indicators for hotspot sources in PG. The ITAI classification map of industrial assessment in the study area can also provide important information for energy efficiency and evaluating eco-environmental quality. which all the other conditions were defined as favourable ecological settings for a healthy environment. Thus, coastal and vegetated areas were removed since they accounted for under ≤ -0.004 at Pasir Gudang (PG) of primary energy use in PM. Thus, they were thought to contribute far less to thermal heat than the three primary categories of industries (Barren land, industrial boundary and Hot-spot sources). The severe IAH phenomenon necessitates a more acceptable industrial zone and industrial development to protect such an eco-environment in Peninsular Malaysia's future industrial strategy, as has been achieved in other similar sectors. PG is the study location with the most surface area affected by adverse industrial activities, accounting for approximately 10% of the total industrial area affected by factory activities. When the entire industrial area was considered, high heat emission affected nearly 3% of the surface at PG, while the rest revealed favourable industrial conditions (Table 10). High heat intensity, on the other hand, affected 10% of the study area compared to its surrounding area, which had a higher percentage of favourable conditions than the industrial area. The coastal and vegetated areas had the most favourable industrial conditions, accounting for nearly 20% of the total metropolitan area covered by the same ITAI classes.

Industrial thermal area index (ITAI)					
Categories No.	Area (km2)	%	ITAI	IAH Phenomenon	industrial assessment index (IAI)
Water body	3.5	20	< -0.000	None	Excellent
Coastal Zone	4.6	26	-0.016 - -0.005	Weak	good
Vegetation	3.6	20	-0.004 – 0.011	Very Weak	Weak
Greenness Area	2.3	13	0.011 – 0.028	Middle	Mid
Barren Land	2.0	11	0.028 – 0.045	Strong	Normal (Intensive)
Industrial boundary	1.3	7	0.045 – 0.067	Stronger	Bad (Very Intensive)
Hot-Spot Sources	0.6	3	> 0.162	Strongest	Worst (Extremely Intensive)

Table 9. The threshold of the industrial assessment index (ITAI) for Pasir Gudang

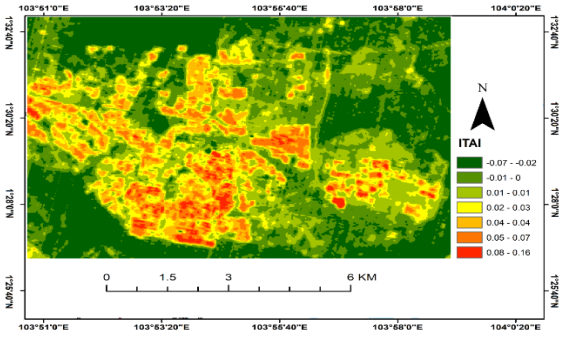

Figure 8. The ITAI classification map of industrial evaluation in Pasir Gudang

4.3. Spatial Distribution of Hot-Spot Classes and IAH Variation

Table 10 and Figure 9 show descriptive statistics for hotspots and their spatial representation. Cool spots are nearly twice as common as hot spots, with average IAH minimum and maximum values ranging from 27.4 °C to 36.2 °C for PG and 3 % of hot-spot areas with IAH values ranging from 55.7 °C to 85.5 °C for PG. Similarly, nearly 19 % of the thermal emission area covers the entire industrial area, and cool spots are nearly twice as numerous as hot spots: 15% of cool spots with average IAH minimum and maximum values ranging from 16.9 °C to 30.1 °C, (Table 9). In contrast, the non-industrial area percentage coverage threshold for PG cool spots exceeded the average industrial area percentage coverage threshold for hot spots. The percentage coverage value of hotspots in 10% of the industrial area was higher than the value in the average non-industrial area. The percentage coverage value of hotspots in 19% of the industrial area was higher than the value in the average non-industrial area.

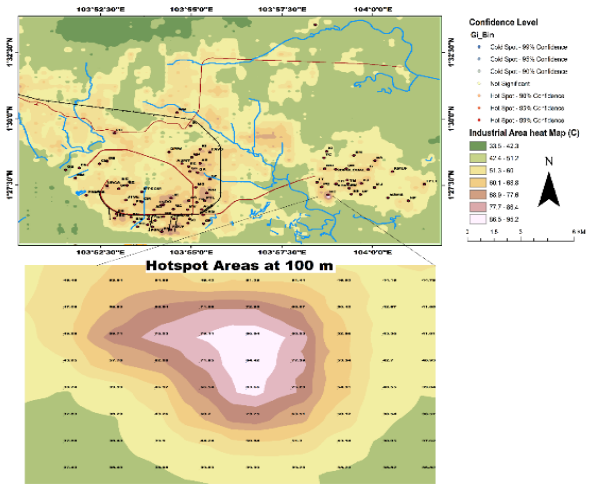

Figure 9. Industrial Area Heat Map shows identified Hotspot targets

Features	Temp. (C)	SA km2	(%)	Gi*Hot-spot Classes		IAH (°C)		
				Gi_Bin	MIN	MAX	MEAN	STD
	< 30	3.5	20	Cold Spot- 99% Confidence	27.4	36.2	34.7	1.2
	36.2 - 39.3	4.6	26	Cold Spot - 95% Confidence	36.2	39.2	37.6	0.9
Pasir Gudang	39.9 - 43.3	3.6	20	Cold Spot - 90% Confidence	39.2	43.3	41.0	1.1
	43.3 - 47.3	2.3	13	Not Significant	43.3	47.3	45.2	1.2
	47.3 - 51.2	2.0	11	Hot Spot - 90% Confidence	47.3	51.2	49.2	1.1
	51.2 - 55.7	1.3	7	Hot Spot -95% Confidence	51.2	55.7	53.1	1.2
	> 85	0.6	3	Hot Spot - 99% Confidence	55.7	84.5	58.5	2.6

Table 10. The percentage coverage area of Getis-Ord Gi* Hot-spot classes with relative average values of IAH PG

4.4 Discussion

Industrial area heat is the energy released in industrial operations at high temperatures from direct combustion processes, at medium temperatures from combustion unit exhaust, and at low temperatures from process unit sections, products, and machinery that is wasted into the environment and serves no useful purpose, Thus, classified as high, medium, or low temperature. The instantaneous heat emission changes of the majority of industrial heat targets, however, as well as their temporal dynamics assessment of the entire region over a year, could be obtained using the rapid RS approach. Certain industrial plants with increasing output over the measuring period were found in the medium industries throughout 2020, using steel and chemical plants as examples. These illustrations demonstrate how heat emissions that reflect the scope of industrial activity can be tracked over time using satellite measurements. Policymakers may receive precise and pertinent information from such efficient trend observations over particular facilities to support dynamic industrial productivity and emission monitoring on finer spatial and temporal dimensions. The simple and quick identification of emissions in industrial operations may also be advantageous to them. The most severe industrial polluters should operate at a lower intensity, according to many researchers, to reduce heat emissions. These industrial sectors should be identified as heat emission risk sources because a small number of super-emitters account for a disproportionately large portion of overall emissions. The thermal heat energy sources and other artificial surfaces experienced high surface temperatures (> 90°C) with precision (RMSE= + 3 °C) based on satellite data. The results show that heat sensing-based IAH estimations can be linearly transferred with only minor accuracy loss. The SW algorithm's IAH estimates differ by no more than 5 °C from the measured air temperature (Rongali, 2018) Greenery surfaces, including sub-industrial areas, had the lowest temperatures (28 39 °C). In addition to the comparison with Landsat-8 data, the IAH of selected targets was confirmed using UAV-based data with the high agreement (R^2 = 0.80 ~ 0.90, p 0.001). Thus, the technique employed is a very concise yet accurate technique for mapping thermal heat energy sources in industrial areas. Maps, models, and hotspot targets from the PG industries were successfully produced using the aerial and satellite-based techniques used in this study. The study's many industrial feature layers, in particular the vegetation state (NDVI), the characteristics of industrial surfaces, and IAH parameters were all related to the degree of thermal significance. The complex hotspot pattern may be explained by the combined and consistent role that various industrial feature layers play during the day in the surface energy balance, which in turn affects how the industrial microclimate behaves. However, vegetation (NDVI) and IAH were the industrial components that were typically identified as significant predictors, as was also the case for cool spots. The presence of vegetation was on average very low, as confirmed by NDVI values < 0.0023, and also a value of VC lower than 50 %. Conversely, hot spots were mostly characterized by high impervious surface (IS) values (10%) for PG associated with low IAH values (1.9 km2) for PG and (13.2 km2), resulting in a high thermal storage capacity. Indeed, IS, as we expected, is the

main driver for IAH increases, as confirmed by other studies (Dahiru et al., 2022; Xia et al., 2018; Zhang et al., 2019; Nanda et al., 2021), and high values could have negative impacts on plant diversity and ecosystem services (Guk & Levin, 2020; Zhou et al., 2019). Hence, it's far more difficult to regulate heat emissions in barren land and industrial zone. Therefore, we concentrated on industrial hot-spot sources, which are important for emerging industries and agents of environmental warming like PG's industrial regions.

4.5 Conclusion

This study connects data on thermal emissions with energy and economic statistics that are far more complicated. It contributes to a better understanding of the relationship between industrialization and environmental consequences, as well as efforts to reduce thermal emissions. This is very common in PG factories that used to be industrial sources of thermal emissions. The findings revealed that industrial emissions are determined by production rather than industrial types, as shown in Figure 9, which generated IAH products with a higher in the medium industry than heavy and light and similarly in UAV, and it can be used in various areas in future research. It can be concluded that by selecting effective dependent variables and formulating appropriate coefficients for variables in the structure of the heat emission equations, the accuracy of the generated data can be improved. Because of its acceptable accuracy, the SW algorithm can be used to derive IAH from the industries in future studies (Sajad Zareie et al., 2018). Future research should focus on improving the accuracy of aerial and satellite IAH generated by split-window algorithms. However, mapping and identifying Hotspot targets will help policymakers and industrial developers become more aware of draught policies and regulations for relevant industries, which will help to close gaps in current industrial activities.

Acknowledgements

The Landsat 8 data from the US Geological Survey (USGS) and UAV data, as well as the Industrial shapefile, are all highly valued in this study. The authors are extremely grateful to the research team (technician and industries planning official), and the INSTeG research desk secretary for their vital participation during this research to improve the original manuscript. The research is supported in part by an MRUN research grant from the Malaysian Ministry of Education (ref: PY/2019/02792), with the vot number -RJ130000.7809.4L881 for this study. The Geoscience & Digital Earth Centre (INSTEG) and the Department of Geoinformatics at Universiti Teknologi Malaysia provided excellent facilities for this project. The Earth Resources Observation System (EROS), the United States Geological Survey's (USGS) data centre, and the National Aeronautics and Space Administration (NASA) are also thanked for the satellite data used in this research.

References

Biswal, S. S., Raval, S., & Gorai, A. K. (2019). Delineation and mapping of coal mine fire using remote sensing data–a review. *International Journal of Remote Sensing*. https://doi.org/10.1080/01431161.2018.1547455

Hazaymeh, K., & Hassan, Q. K. (2015). Spatiotemporal image-fusion model for enhancing the temporal resolution of Landsat-8 surface reflectance images using MODIS images. *Journal of Applied Remote Sensing*, *9*(1), 096095. https://doi.org/10.1117/1.jrs.9.096095

Heutger, M. (2014). Unmanned Aerial Vehicles in Logistics (DHL Perspective). Retrieved from http://www.dhl.com/content/dam/downloads/g0/about_us/logistics_insights/DHL_TrendReport_UAV.pdf

Industrial Heat Sources Detection Method Based on thermal Infrared Satellite Data.pdf. (n.d.).

Kant, P. M. (2021). Geothermal mapping and remote sensing of surface thermal anomalies at Grændalur University of Iceland Geothermal mapping and remote sensing of surface thermal anomalies at Grændalur area, Hveragerði , SW Iceland.

Kuenzer, C., Dech, S., Arvidson, T., Barsi, J., Jhabvala, M., & Reuter, D. (2013). *Thermal Infrared Remote Sensing*. *Thermal Infrared Remote Sensing: Sensors, Methods, Applications* (Vol. 17). https://doi.org/10.1007/978-94-007-6639-6

Liu, Y., Hu, C., Zhan, W., Sun, C., Murch, B., & Ma, L. (2018). Identifying industrial heat sources using the time series of the VIIRS Nightfire product with an object-oriented approach. *Remote Sensing of Environment*, *204*(February 2017), 347–365. https://doi.org/10.1016/j.rse.2017.10.019

Malakar, N. K., Hulley, G. C., Hook, S. J., Laraby, K., Cook, M., & Schott, J. R. (2018). An Operational Land Surface Temperature Product for Landsat Thermal Data: Methodology and Validation. *IEEE Transactions on Geoscience and Remote Sensing*, *56*(10), 5717–5735. https://doi.org/10.1109/TGRS.2018.2824828

Mia, M. B., Fujimitsu, Y., & Nishijima, J. (2017). Thermal Activity Monitoring of an Active Volcano Using Landsat 8/OLI-TIRS Sensor Images: A Case Study at the Aso Volcanic Area in Southwest Japan. *Geosciences (Switzerland)*, *7*(4). https://doi.org/10.3390/geosciences7040118

Murad, D. L. M. R., Nasir, M. S. M., Law, L. C., Idris, I., & Othman, M. R. (2019). Flared gas emission control from an oil production platform. *Journal of Physical Science*, *30*, 125–147. https://doi.org/10.21315/jps2019.30.s1.8

Omotosho, T. V., Emetere, M. E., Akinyemi, M. L., Abdullah, M., & Mandeep, J. S. (2015). Mathematical investigations of gas flare constituents in oil-producing regions of Malaysia. *International Conference on Space Science and Communication, IconSpace*, *2015-Septe*, 111–116. https://doi.org/10.1109/IconSpace.2015.7283754

Pandya, M. R., Shah, D. B., Trivedi, H. J., Darji, N. P., Ramakrishnan, R., Panigrahy, S., … Kirankumar, A. S. (2014). Retrieval of land surface temperature from the Kalpana-1 VHRR data using a single-channel algorithm and its validation over western India. *ISPRS Journal of Photogrammetry and Remote Sensing*, *94*, 160–168. https://doi.org/10.1016/j.isprsjprs.2014.05.004

Pour, A. B., Park, T. Y. S., Park, Y., Hong, J. K., Muslim, A. M., Läufer, A., … Hossain, M. S. (2019). *Landsat-8, advanced spaceborne thermal emission and reflection radiometer, and WorldView-3 multispectral satellite imagery for prospecting copper-gold mineralization in the northeastern Inglefield Mobile Belt (IMB), northwest Greenland*. *Remote Sensing* (Vol. 11).

https://doi.org/10.3390/rs11202430

Storey, J., Choate, M., & Lee, K. (2014). Landsat 8 operational land imager on-orbit geometric calibration and performance. *Remote Sensing*, *6*(11), 11127–11152. https://doi.org/10.3390/rs61111127

Vollath, D. (1987). Automatic focusing by correlative methods. *Journal of Microscopy*, *147*(3), 279–288. https://doi.org/10.1111/j.1365-2818.1987.tb02839.x

Xia, H., Chen, Y., & Quan, J. (2018). A simple method based on the thermal anomaly index to detect industrial heat sources. *International Journal of Applied Earth Observation and Geoinformation*, *73*(June), 627–637. https://doi.org/10.1016/j.jag.2018.08.003

Yang, Y., Li, X., Pan, X., Zhang, Y., & Cao, C. (2017). Downscaling land surface temperature in complex regions by using multiple scale factors with adaptive thresholds. *Sensors (Switzerland)*, *17*(4). https://doi.org/10.3390/s17040744

Zhang, P., Yuan, C., Sun, Q., Liu, A., You, S., Li, X., … Lun, F. (2019). Satellite-Based Detection and Characterization of Industrial Heat Sources in China. *Environmental Science and Technology*, *53*(18), 11031–11042. https://doi.org/10.1021/acs.est.9b02643